LETTER

doi:10.1038/nature13493

Pathway from subducting slab to surface for melt and fluids beneath Mount Rainier

R Shane McGary[1], Rob L. Evans[1], Philip E. Wannamaker[2], Jimmy Elsenbeck[1] & Stéphane Rondenay[3]

Convergent margin volcanism originates with partial melting, primarily of the upper mantle, into which the subducting slab descends[1,2]. Melting of this material can occur in one of two ways. The flow induced in the mantle by the slab can result in upwelling and melting through adiabatic decompression[1,3]. Alternatively, fluids released from the descending slab through dehydration reactions can migrate into the hot mantle wedge, inducing melting by lowering the solidus temperature[2,4]. The two mechanisms are not mutually exclusive[1]. In either case, the buoyant melts make their way towards the surface to reside in the crust or to be extruded as lava. Here we use magnetotelluric data collected across the central state of Washington, USA, to image the complete pathway for the fluid–melt phase. By incorporating constraints from a collocated seismic study[5] into the magnetotelluric inversion process, we obtain superior constraints on the fluids and melt in a subduction setting. Specifically, we are able to identify and connect fluid release at or near the top of the slab, migration of fluids into the overlying mantle wedge, melting in the wedge, and transport of the melt/fluid phase to a reservoir in the crust beneath Mt Rainier.

Despite important efforts to understand the production and transport of fluid and melt phases in subduction zones, a number of outstanding questions remain. Do fluids released from the slab rise vertically into the mantle wedge[2], or are ascent paths more complex[6–8]? Do the fluids migrate into the mantle wedge by reactive porous flow[1,9] or more quickly by way of fractures[2], channelling[8,10] or diapirism[3]? Is the location of the volcanic arc defined by the location of melting above the anhydrous solidus[11], aqueous fluid connectivity in the mantle wedge[12], or some combination of kinematic variables such as slab dip and convergence rate with fluid transport[13]? Better constraints on the fluid transport pathways within the subduction setting are needed to address these questions.

The CAFE (Cascadia Array for Earthscope) experiment was designed to collect co-located seismic and magnetotelluric data from instrumentation deployed along a dense west–east transect across central Washington (Fig. 1). The seismic results have been addressed previously[5,14], and here the magnetotelluric results are presented. Data were collected at 60 wideband and 20 long-period magnetotelluric stations, with generally good-quality responses over the period range from ~0.005 s to ~8000 s. The data are consistent with a two-dimensional, north–south-striking resistivity structure[15,16], which we determined through a two-dimensional nonlinear conjugate-gradient inversion[17] (see Methods).

The magnetotelluric method is attractive for use in subduction settings because it is particularly sensitive to electrically conductive fluid and melt phases and can therefore be used to illuminate fluid processes and pathways in the subduction zone. The magnetotelluric method has been used to good effect in a number of subduction settings, including Cascadia[18–21]. For the CAFE data, we were able to augment the magnetotelluric image by incorporating results from the seismic project directly into the magnetotelluric inversion process.

Results for both the seismic and magnetotelluric experiments are shown in Fig. 2. The velocity increase in the dipping low-velocity layer in the seismic image at depths of about ~40–45 km depth at the top of the subducting layer is interpreted to reflect the transition of the hydrated basalts of the upper crust towards eclogite. The disappearance of that layer at depths of 75–90 km is further interpreted to result from the transition of lower-crustal metastable gabbro into eclogite. This reaction would be accelerated by fluids released from the dehydration of serpentine or chlorite in the subducting upper-mantle harzburgite[22], a conclusion supported by local earthquake hypocentre evidence[23]. The low-velocity feature above the subducting slab at depths of 65–80 km is interpreted as a fluid/melt phase resulting from the release of fluids from the slab[5].

The magnetotelluric results are consistent with the seismic interpretation, but develop our understanding of the subduction process much further. The most prominent magnetotelluric structure is the highly conductive (2–5 Ω m) region (A) near the top of the slab in the magnetotelluric model, coincident with the low-velocity fluid/melt feature in the seismic image. This conductor probably cannot be explained by dry melting alone as resistivities $<5\,\Omega\,m$ would require excessively high melt fractions[24]. Additionally, the temperatures near the top of the slab at this depth are roughly 1,100 °C–1,150 °C (ref. 25) more than 200 °C below the dry peridotite solidus[1]. Both of these difficulties are resolved by the addition of water released from the slab. As little as 0.2 wt% water dissolved into the peridotite is sufficient to reduce the solidus temperature to below the temperatures found at the slab surface[1,8], which would allow flux melting to occur[13]. An incipient melt fraction of 2% would equate to 10 wt% water in the melt, enough to account for a resistivity of 2 Ω m (Fig. 3).

The calculations for fluid content assume that the fluid/melt phases are well connected. Interconnection along grain edges in a peridotite matrix requires a dihedral angle of $<60°$. At 25 kbar, this occurs at temperatures above 950 °C (ref. 12), which is achieved in the region of interest. Although higher temperatures are required to maintain a sufficiently

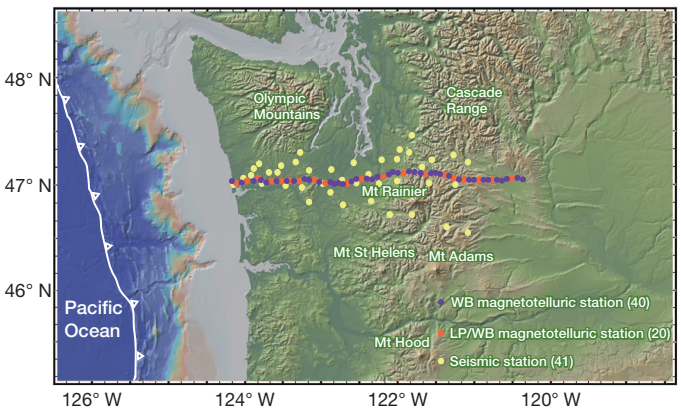

Figure 1 | Map showing station locations for the CAFE seismic and magnetotelluric stations (wideband and long-period) across central Washington state, USA. The numbers in parentheses indicate the number of stations for each category. WB, wideband; LP, long-period.

[1]Department of Geology and Geophysics, MS#22, Woods Hole Oceanographic Institution, 360 Woods Hole Road, Woods Hole, Massachusetts 02543, USA. [2]Energy and Geoscience Institute, University of Utah, 423 Wakara Way, Suite 300, Salt Lake City, Utah 84108, USA. [3]Department of Earth Science, University of Bergen, Allegaten 41, 5007 Bergen, Norway.

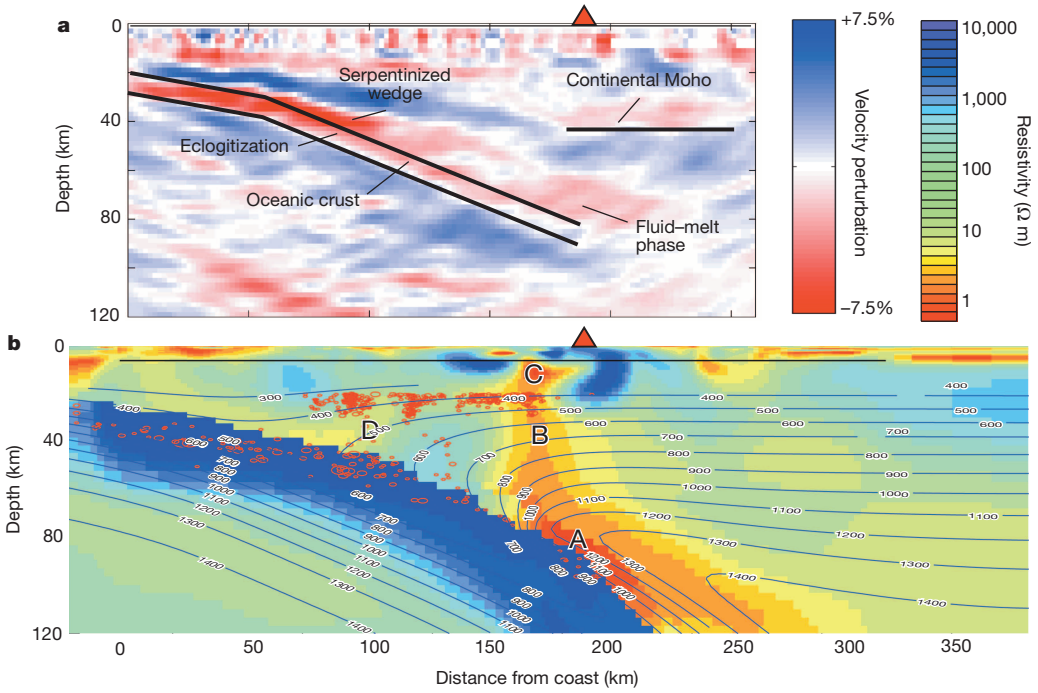

Figure 2 | Primary seismic (a) and magnetotelluric (b) models. Panel **b** includes both a thermal profile (contours, labelled in degrees Celsius) and earthquake hypocentre locations (red circles) within 20 km of our profile line[23]. Fluid released from the subducting slab enters the mantle wedge at A. Melt initiated at or very near the interface is transported upward by buoyancy and dragged down. The fluid/melt phase rises through the mantle wedge (B) until it reaches the crust, joining fluids released from shallower reactions (D). The combined fluid/melt continues to rise until reaching a reservoir (C) in the crust. Mount Rainier is shown as a red triangle.

small dihedral angle at shallower depths, melt should become directly interconnected once the melt fraction exceeds 2 vol.% (ref. 26), ensuring that the fluid/melt phase remains well connected during ascent as the water-rich initial melt reacts with the overlying mantle[4].

Our model cannot determine whether melting starts at the top of the slab or some short distance away, as the solidus for hydrated peridotite and the temperatures expected at the top of the slab are very close[1,25]. However, yttrium concentrations in the range 13–19 parts per million (p.p.m.) in samples of Mt Rainier andesite suggest that some melting does occur at the interface and even within the slab for Cascadia[27,28].

In either case, the buoyant fluid and melt phases are gravitationally unstable and can rise through the mantle wedge diapirically[3]. It has also been argued that the trajectories for these instabilities may not necessarily be vertical, as the subduction induced motion in the mantle wedge would tend to drag them towards the hot corner of the wedge[7]. Both types of migration may be apparent in the magnetotelluric model (Fig. 2b), with the conductor extending from the primary source (A) both upwards into the mantle and sub-horizontally away from the slab. Additionally, the sub-horizontal extension could simply represent an extended zone of fluid release from the slab.

Although the incipient melt is very water-rich, it becomes diluted as it rises and further decompressional melting occurs[8]. This tradeoff would result in a slight increase in the bulk resistivity, for example, at 1,150 °C the resistivity of peridotite bearing a 2.5 vol.% melt with 10% water content is about 2 Ω m, whereas the resistivities as the melt fraction rises to 5 vol.% (5 wt% water content) and 10 vol.% (2.5 wt% water content) are about 3.5 Ω m and about 5 Ω m respectively (Fig. 3), ignoring the effects of water on bulk mantle. This is consistent with structure within the mantle wedge in the magnetotelluric model (feature B in Fig. 2b). This conductor maintains a resistivity of 5–6 Ω m throughout its ascent within the mantle. Figure 3 shows the effect of melt fraction and water content on the conductivity of the melt-bearing peridotite at 1,150 °C. Conductivities fall rapidly with decreasing temperature for a given combination of melt fraction and water content, suggesting that the resistivities seen in the image appear to rule out any significant temperature decrease (the thermal model superimposed on the image is a steady-state solution that does not factor in thermal energy transported by rising melt). This result argues for a relatively rapid vertical transit for the melt, possibly through large diapirs or interconnected conduits.

The ascending melt appears to rise until it reaches a reservoir in the crust (C), after being joined by fluids presumably originating from a conductor (D) associated with the dehydration of hydrated metabasalt in the upper-crustal layer of the descending slab[5]. Conductor C is in the same position as a conductor identified as the Southern Washington Cascades Conductor in earlier studies[21,29], and similar conductors appear to be a ubiquitous feature in subduction settings[30]. It has been argued that this crustal reservoir represents metasediments[21] or collected fluids[30], and this clearly seems to be the case in Oregon (and undoubtedly elsewhere) where the temperature of the fluid source is only about 500 °C. In the CAFE line, however, we can clearly see that the conditions for mantle melting are met. This does not rule out the possible presence of metasediments which may explain the small shallow conductor west of C, or even part of the conductive signature of C itself.

A conductor similar to D has also been identified previously in central Oregon[20]. In the Oregon image, this conductor appeared to be the primary source of fluid connected to the crustal conductor, whereas in the CAFE line it is clearly a secondary source, with a much stronger contribution coming from the rising melt. Three-dimensional inversions

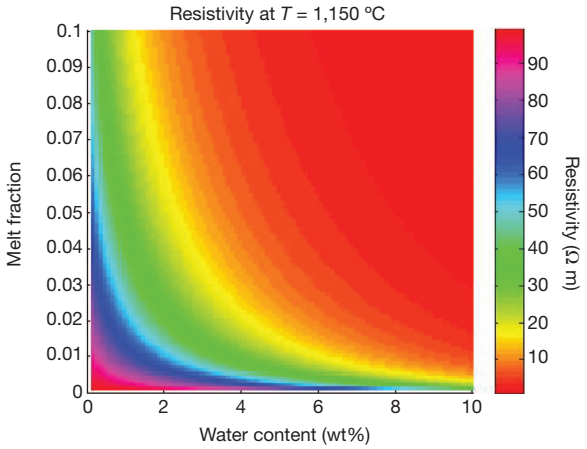

Figure 3 | The resistivity of peridotite for a given melt fraction and water content (within the melt) at a temperature of 1,150 °C. The method used for the calculation of resistivities is that given in ref. 24.

of regional magnetotelluric[21] data at a coarser resolution than our data set corroborate our model by showing a strong conductor rising from the slab in this region, but also highlight the substantial along-strike variability in deep melt production in Cascadia. We suggest that this variability relates to first-order differences in the hydration of the incoming plate, with a wetter slab present beneath the CAFE line. Illuminating the differences in fluid release and melt generation brings us one step closer to understanding the connections between fluid release and seismogenic and volcanic processes operative in these critical tectonic settings.

METHODS SUMMARY

The CAFE magnetotelluric experiment comprised a dense linear array of 60 wideband (spaced at about 5-km intervals) and 20 long-period (spaced at about 15-km intervals) magnetotelluric instruments. The former were acquired through contract from the University of Utah to Quantec Geoscience, Inc., while the latter were acquired by P.E.W. and student/post-doc crew using Narod Intelligent Magnetotelluric System (NIMS) instruments then owned by the University of Washington as part of the Electromagnetic Studies of the Continents (EMSOC) pool. The magnetotelluric array passes in an east–west line through the earlier CAFE seismic profile.

The long-period and wideband magnetotelluric data were processed using robust methods[31,32] with two separate remote reference sites (one reference was over 500 km away). Combined, the instruments yielded magnetotelluric response functions typically over the period range of 0.005 s to 8000 s.

Multi-site, multi-frequency Groom–Bailey tensor decomposition[15,16] was used to determine strike direction and viability of a two-dimensional inversion, and to separate from the impedance tensor distortion elements affecting both amplitude and phase of the electric field.

We generated our two-dimensional models of resistivity structure using the WinGLink inversion algorithm[17]. The inversions started with a 100 Ω m half-space, excepting the ocean, fixed at 0.33 Ω m and defined by local bathymetry, and a dipping resistor representing the upper part of the subducting slab whose location was defined by constraints from the seismic migration results. A tear zone (allowing sharp conductivity transitions) was imposed at the top of the dipping resistor. Extensive testing for sensitivity and robustness was performed on significant features by removing features from the model and re-running the inversion, and by varying parameters such as resistivity or extent of a feature in a systematic way and observing the effect on the misfit between the data and model. The incorporation of seismic constraints into the magnetotelluric inversion constitutes a novel approach and enables superior imaging of fluids in the subduction setting.

Online Content Methods, along with any additional Extended Data display items and Source Data, are available in the online version of the paper; references unique to these sections appear only in the online paper.

Received 6 December 2013; accepted 15 May 2014.

1. Stern, R. J. Subduction zones. *Rev. Geophys.* **40,** 1012, http://dx.doi.org/10.1029/2001RG000108 (2002).
2. Davies, J. H. & Stevenson, D. J. Physical model of source region of subduction zone volcanics. *J. Geophys. Res.* **97** (B2), 2037–2070 (1992).
3. Hall, P. S. & Kincaid, C. Diapiric flow at subduction zones: a recipe for rapid transport. *Science* **292,** 2472–2475 (2001).
4. Grove, T. L., Chatterjee, N., Parman, S. W. & Medard, E. The influence of H_2O on mantle wedge melting. *Earth Planet. Sci. Lett.* **249,** 74–89 (2006).
5. McGary, R. S. The CAFE experiment: a joint seismic and MT investigation of the Cascadia subduction system. PhD thesis, MIT/WHOI Joint Program (2013).
6. Schurr, B., Asch, G., Rietbrock, A., Trumbull, R. & Haberland, C. Complex patterns of fluid and melt transport in the central Andean subduction zone revealed by attenuation tomography. *Earth Planet. Sci. Lett.* **215,** 105–119 (2003).
7. Marschall, H. R. & Schumacher, J. C. Arc magmas sourced from mélange diapirs in subduction zones. *Nature Geosci.* **5,** 862–867 (2012).
8. Pearce, J. A. & Peate, D. W. Tectonic implications of the composition of volcanic arc magmas. *Annu. Rev. Earth Planet. Sci.* **23,** 251–285 (1995).
9. Navon, O. & Stolper, E. Geochemical consequences of melt percolation: the upper mantle as a chromatographic column. *J. Geol.* **95,** 285–307 (1987).
10. Daines, M. J. & Kohlstedt, D. L. The transition from porous to channelized flow due to melt/rock reaction during melt migration. *Geophys. Res. Lett.* **21,** 145–148 (1994).
11. England, P. C. & Katz, R. F. Melting above the anhydrous solidus controls the location of volcanic arcs. *Nature* **467,** 700–703 (2010).
12. Mibe, K., Yoshino, T., Ono, S., Yasuda, A. & Fujii, T. Connectivity of aqueous fluid in eclogite and its implications for fluid migration in the Earth's interior. *J. Geophys. Res.* **108** (B6), 2295, http://dx.doi.org/10.1029/2002JB001960 (2003).
13. Grove, T. L., Till, C. B., Lev, E., Chatterjee, N. & Medard, E. Kinematic variables and water transport control the formation and location of arc volcanoes. *Nature* **459,** 694–697 (2009); erratum **460,** 1044 (2009).
14. Abers, G. A. *et al.* Imaging the source region of Cascadia tremor and intermediate-depth earthquakes. *Geology* **37,** 1119–1122 (2009).
15. McNeice, G. W. & Jones, A. G. Multisite, multifrequency tensor decompositions of magnetotelluric data. *Geophysics* **66,** 158–173 (2001).
16. Groom, R. W. & Bailey, R. C. Decomposition of magnetotelluric impedance tensors in the presence of local three-dimensional galvanic distortion. *J. Geophys. Res.* **94,** 1913–1925 (1989).
17. Rodi, W. L. & Mackie, R. L. Nonlinear conjugate gradients algorithm for 2-D magnetotelluric inversion. *Geophysics* **66,** 174–187 (2001).
18. Wannamaker, P. E. *et al.* Resistivity cross section through the Juan de Fuca subduction system and its tectonic implications. *J. Geophys. Res.* **94,** 14127–14144 (1989).
19. Soyer, W. & Unsworth, M. Deep electrical structure of the northern Cascadia (British Columbia, Canada) subduction zone: implications for the distribution of fluids. *Geology* **34,** 53–56 (2006).
20. Evans, R. L., Wannamaker, P., McGary, R. S. & Elsenbeck, J. Electrical structure of the Central Cascadia subduction zone: the EMSLAB Lincoln line revisited. *Earth Planet. Sci. Lett.* http://dx.doi.org/10.1016/j.epsl.2013.04.021 (in the press).
21. Meqbel, N. M., Egbert, G. D., Wannamaker, P. E., Kelbert, A. & Schultz, A. Deep electrical resistivity structure of the northwestern U.S. derived from 3-D inversion of USArray magnetotelluric data. *Earth Planet. Sci. Lett.* http://dx.doi.org/10.1016/j.epsl.2013.12.026 (in the press).
22. John, T. & Schenk, V. Partial eclogitization of gabbroic rocks in a late Precambrian subduction zone (Zambia): prograde metamorphism triggered by fluid infiltration. *Contrib. Mineral. Petrol.* **146,** 174–191 (2003).
23. McCrory, P. A., Blair, J. L., Waldhauser, F. & Oppenheimer, D. H. Juan de Fuca slab geometry and its relation to Wadati-Benioff zone seismicity. *J. Geophys. Res.* **117,** B09306 (2012).
24. Ni, H., Keppler, H. & Behrens, H. Electrical conductivity of hydrous basaltic melts: implications for partial melting in the upper mantle. *Contrib. Mineral. Petrol.* **162,** 637–650 (2011).
25. van Keken, P. E., Hacker, B. R., Syracuse, E. M. & Abers, G. A. Subduction factory: 4. Depth-dependent flux of H_2O from subducting slabs worldwide. *J. Geophys. Res.* **116,** B01401 (2011).
26. Zhu, W., Gaetani, G. A., Fusseis, F., Montesi, L. G. J. & De Carlo, F. Microtomography of partially molten rocks: three-dimensional melt distribution in mantle peridotite. *Science* **332,** 88–91 (2011).
27. Defant, M. J. & Drummond, M. S. Derivation of some modern arc magmas by melting of young subducted lithosphere. *Nature* **347,** 662–665 (1990).
28. Stockstill, K. R., Vogel, T. A. & Sisson, T. W. Origin and emplacement of the andesite of Burroughs Mountain, a zoned, large-volume lava flow at Mount Rainier, Washington, USA. *J. Volcanol. Geotherm. Res.* **119,** 275–296 (2003).
29. Egbert, G. D. & Booker, J. R. Imaging crustal structure in southwestern Washington with small magnetometer arrays. *J. Geophys. Res.* **98** (B9), 15967–15985 (1993).
30. Worzewski, T., Jegen, M., Kopp, H., Brasse, H. & Castillo, W. T. Magnetotelluric image of the fluid cycle in the Costa Rican subduction zone. *Nature Geosci.* **4,** 108–111 (2011).
31. Chave, A. D. & Thompson, D. J. Bounded influence magnetotelluric response function estimation. *Geophys. J. Int.* **157,** 988–1006 (2004).
32. Egbert, G. D. Robust multiple station magnetotelluric data processing. *Geophys. J. Int.* **130,** 475–496 (1997).

Acknowledgements We thank V. Maris, M. Brown, A. Kelbert, and Quantec Geoscience, Inc. for their part in data acquisition. We also thank A. Pommier, D. Lizarralde, A. Malcolm, A. Shaw, H. Marschall and J. P. Canales for critical discussions and input on early versions of the manuscript. Finally, we thank P. van Keken for use of his thermal overlay in the magnetotelluric figure. This work was supported by US National Science Foundation grant EAR08-44041 (Principal Investigator R.L.E.) and US National Science Foundation grant EAR08-43725 (Principal Investigator P.E.W.), both through the Earthscope programme. R.S.M. was supported by a National Defense Science and Engineering Graduate (NDSEG) fellowship.

Author Contributions R.L.E. and P.E.W. conceived the experiment. R.S.M. participated in data collection and was primarily responsible for the processing and inversion work and analysis. R.L.E. was involved in all aspects of the development of the magnetotelluric models. P.E.W. coordinated and led the data collection, and also performed some of the processing and analysis of the broadband data. J.E. assisted with data reduction and processing. S.R. was involved in the production of the seismic image. All authors contributed to the understanding of the results and editing of the manuscript.

Author Information Reprints and permissions information is available at www.nature.com/reprints. The authors declare no competing financial interests. Readers are welcome to comment on the online version of the paper. Correspondence and requests for materials should be addressed to R.S.M. (mcgaryr@tcnj.edu).

METHODS

Time series data for the CAFE magnetotelluric project were collected at 20 long-period and 60 wideband sites. The long-period data were collected using NIMS instruments with each station in place for typically three weeks. The wideband data were collected using Phoenix Geosystems instruments, with a typical recording interval of 15 h for each site. The entire array was 280 km in length, and designed to be roughly collocated with the earlier CAFE passive seismic experiment.

The time series data from each long-period station were visually inspected for breaks, trends, and signal-to-noise ratio, and then windowed with data from two separate magnetic remote reference sites. One remote reference for each station was chosen from distant CAFE magnetotelluric stations, and the second concatenated from Earthscope/USArray stations that were operated simultaneously in Nevada and California, with a minimum distance of 500 km between stations to ensure that the noise between the stations was not likely to be correlated to any significant degree. Dual remote references were also used for the wideband data, with one remote reference located approximately 30 km east of Mt Rainier, and the other in Buena Vista Valley, Nevada.

The long-period time series data were processed into impedance tensors using the robust bounded influence remote reference processing (BIRRP) algorithm[31]. The wideband data were also processed using robust methods[32]. The long-period transfer functions provided useful data from ten seconds up to several thousand seconds, and the wideband transfer functions provided useful data from less than one second up to several hundred.

Dimensionality and regional strike direction were evaluated for the data in a variety of ways, including phase tensor analysis[33], Bahr skew analysis[34], and multi-site, multi-frequency Groom–Bailey tensor decomposition using the Strike software package[15,16]. The phase tensor ellipses show a consistent pattern for periods between 10 s and 2,000 s, with a near north–south strike for stations west of Mt Rainier, shifting to a slightly clockwise strike to the east of Mt Rainier, with a more pronounced clockwise shift for stations towards the eastern end of the profile. This is consistent with previous strike analysis conducted on a set of Earthscope long-period stations along a line at roughly 46.5° N (ref. 35).

Bahr (phase-sensitive) skew analysis provides a justification for a two-dimensional analysis of the data between the same periods, with exceptions beneath stations LP-32 and LP-36 (immediately west of Mt Rainier) for periods greater than 400 s, and beneath stations LP-44 (just east of Mt Rainier) and LP-54 (in a river valley just north of Ellensburg) for periods less than 150 s.

Using the Strike algorithm[15], we determined that a regional strike direction of seven degrees west of north provided the best χ-squared fit for the long-period data for periods of 100–1,350 s, within confidence intervals when stations LP-32 and LP-36 were excluded. A strike direction of due north also produced an acceptable fit, and was used in the inversions. The strike angles for the entire set of decomposed transfer functions are displayed in Extended Data Fig. 1.

To generate our regularized two-dimensional models of resistivity structure, we used the nonlinear conjugate gradient inversion algorithm WinGLink[17]. Our inversion mesh consisted of 116 rows and 234 columns, with a very fine row height near the surface increasing gradually with depth, and a column width that was maintained to be generally uniform to the extent allowed by station spacing. One set of inversions were run starting with a half-space of 100 Ω m, except for the ocean, which was fixed at 0.33 Ω m with an extent defined by local bathymetry. A second set of inversions additionally incorporated a tear zone at the top of the slab, with the location determined by the seismic migration profile, and an imposed resistive feature (5,000 Ω m) that represents the slab, extending approximately 30 km below the slab surface. Although this feature was imposed on the incipient inversion model, it was not locked and was free to evolve during the inversion process. It has been shown that the tear zone and imposition of this resistive feature will produce a significantly more accurate image of nearby conductive fluids, particularly if these fluids are released at or near the slab surface[5]. The inversion model generated without the imposed tear is displayed as Extended Data Fig. 2. The same technique has been used to invert data in Cascadia and other subduction zones[20,36].

The τ value determines the tradeoff between smoothness and misfit in the inversion, and we determined a τ value of 3.3 to be optimal. Two other parameters, α and β, define the relationship of the smoothness parameter in the vertical as compared to the horizontal, and the way in which smoothness changes with depth respectively. A range of values from 0.8 to 1.8 for α and 1.0 to 2.0 for β were evaluated, with the final selected values of 1.5 and 1.7 respectively. These values are consistent with values used in inversions of other similar data sets[20]. While small changes in α and β have been shown to produce striking differences in structure in some cases[36], the changes that we saw in structure when varying these parameters was quite minimal. It should also be noted that the same parameter values were used in generating both final images, that is, with and without the tear imposed.

We generated models that inverted both the transverse magnetic (TM) and transverse electric (TE) modes, with error floors of 5% and 15% respectively, and a set of models using only the TM mode. The tipper function was included in both sets of models, and was also evaluated separately, clearly supporting the presence of the vertical conductor.

We also evaluated the extent to which the primary structures in our models were supported and/or required by the data. This was done in a number of ways, such as assessing how the structures were affected by parameter modifications as described above, and comparing the resulting models to the data pseudo-sections (included as Extended Data Fig. 3) to give us a better understanding of how data from each station might be affecting the inversion.

Additionally, we used manual editing techniques. This involved removing or altering a feature in the resultant model and then allowing the inversion process to seek a solution optimally close to this altered model. If the feature was restored by the inversion, it was taken to be required by the data. If the inversion was able to achieve a misfit comparable to the original misfit without restoring the feature, the structure in question was determined to be allowed but not required by the data. For our final models, all three major conductive features, the slab top, the vertical column, and the crustal conductor were found to be required by the data using these methods.

We achieved a root-mean-square misfit value of 1.89 for the inversion using the tear, as compared to 3.08 for the halfspace. A plot of root-mean-square misfit by station (Extended Data Fig. 4) shows that while the model with the tear shows improvement in fit for almost every station, the effect is much more pronounced between stations 30 and 55, which correspond to horizontal distances of 150–275 km from the coast. By far the most striking differences between the two models in this range is that for the model with the tear, the conductor is more intense and not separated from the resistive slab by any significant distance. Taken together, this strongly suggests that the model with the tear is significantly more accurate, and that the imposed smoothness is largely responsible for the higher misfit in the half-space model. We note that although the geometry of this data set is not optimized for a three-dimensional treatment, inversions of the regional Earthscope Transportable Array data collected on a ~70-km grid, confirms the presence of the large conductor emanating from the slab[35], although the resolution of the three-dimensional model is necessarily coarser than that in our model.

33. Caldwell, T. G., Bibby, H. M. & Brown, C. The magnetotelluric phase tensor. *Geophys. J. Int.* **158,** 457–469 (2004).
34. Simpson, F. & Bahr, K. *Practical Magnetotellurics* 93–98 (Cambridge Univ. Press, 2005).
35. Patro, P. K. & Egbert, G. D. Regional conductivity structure of Cascadia: preliminary results from 3D inversion of USArray transportable array magnetotelluric data. *Geophys. Res. Lett.* **35,** L20311 (2008).
36. Matsuno, T. *et al.* Upper mantle electrical resistivity structure beneath the central Mariana subduction system. *Geochem. Geophys. Geosyst.* **11,** Q09003 (2010).

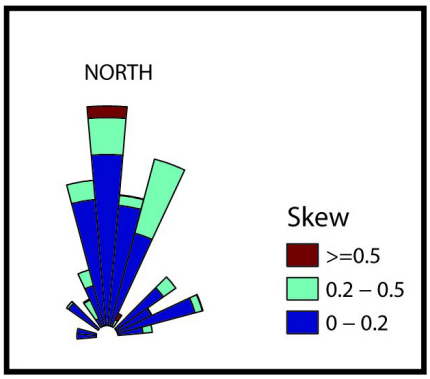

Extended Data Figure 1 | Rose diagram showing overall strike directions. The colour code reflects the Bahr skew as determined using the STRIKE algorithm[15] for the CAFE data set.

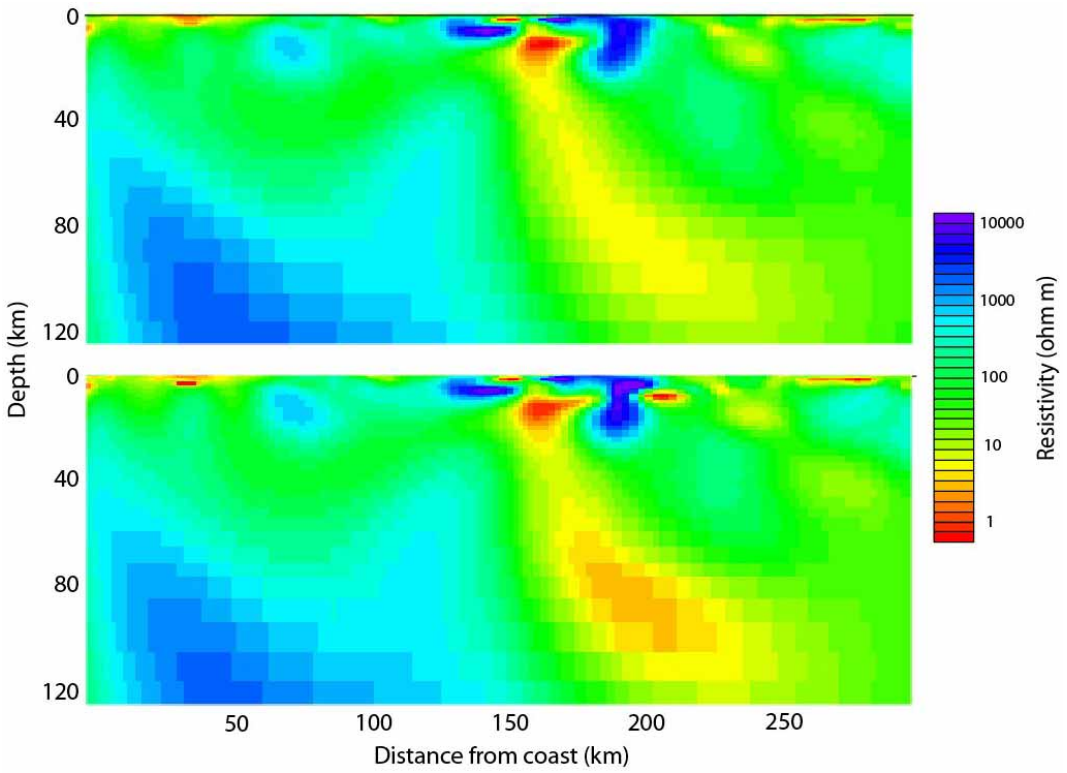

Extended Data Figure 2 | Primary standard inversion images for the CAFE data. These magnetotelluric images were generated without incorporating a tear zone on top of the slab or setting the initial resistivity for the slab. The top image was generated using a combination of the TM mode and tipper, whereas the bottom image was produced using the TM and TE modes along with the tipper.

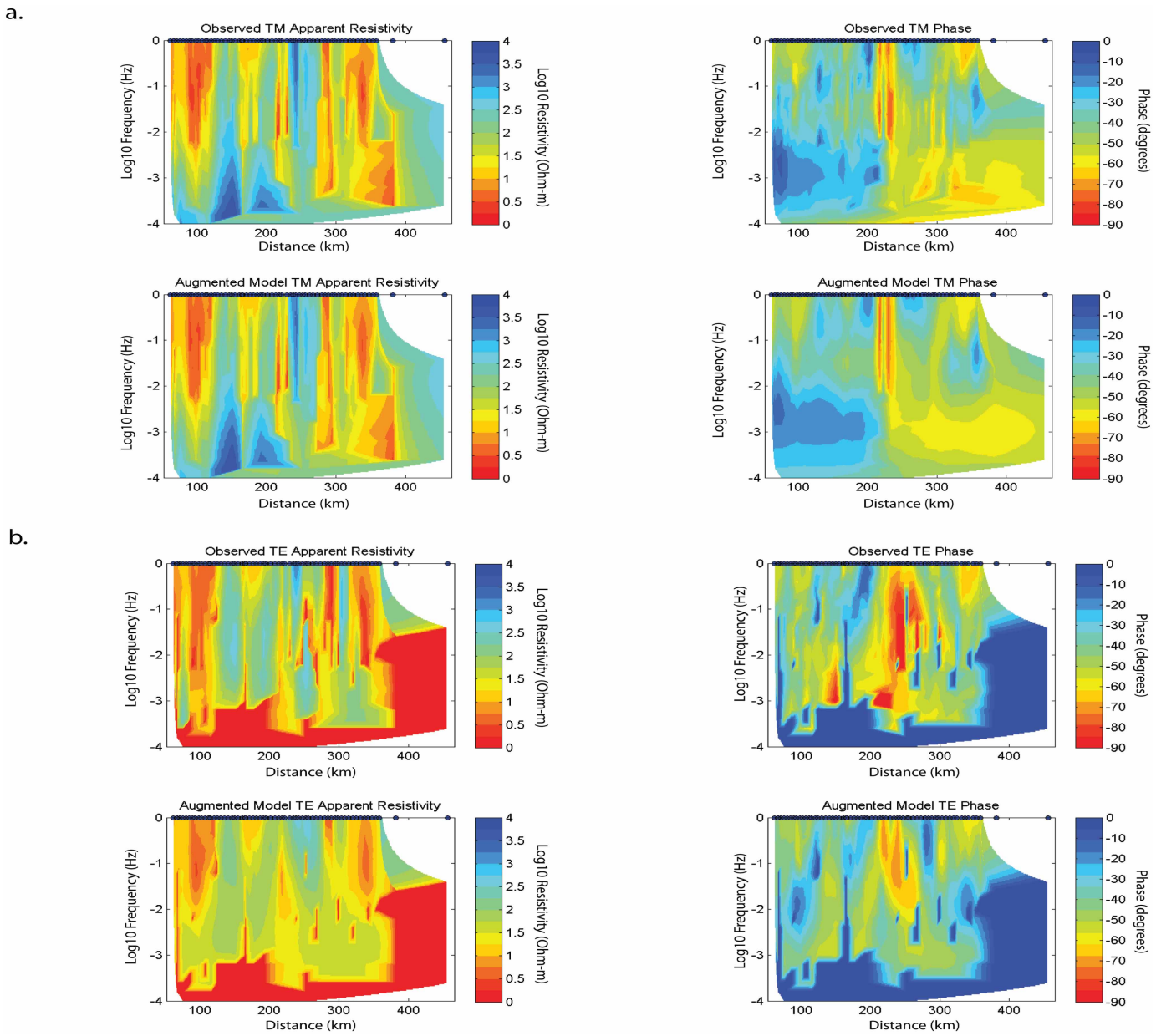

Extended Data Figure 3 | The TM (a) and TE (b) pseudo-sections for the CAFE magnetotelluric data. The two upper panels in **a** and the two upper panels in **b** show apparent resistivity and phase for the data. The two lower panels in **a** and the two lower panels in **b** show apparent resistivity and phase for the model. Both models are limited horizontally to correspond with the surface covered by the CAFE magnetotelluric array.

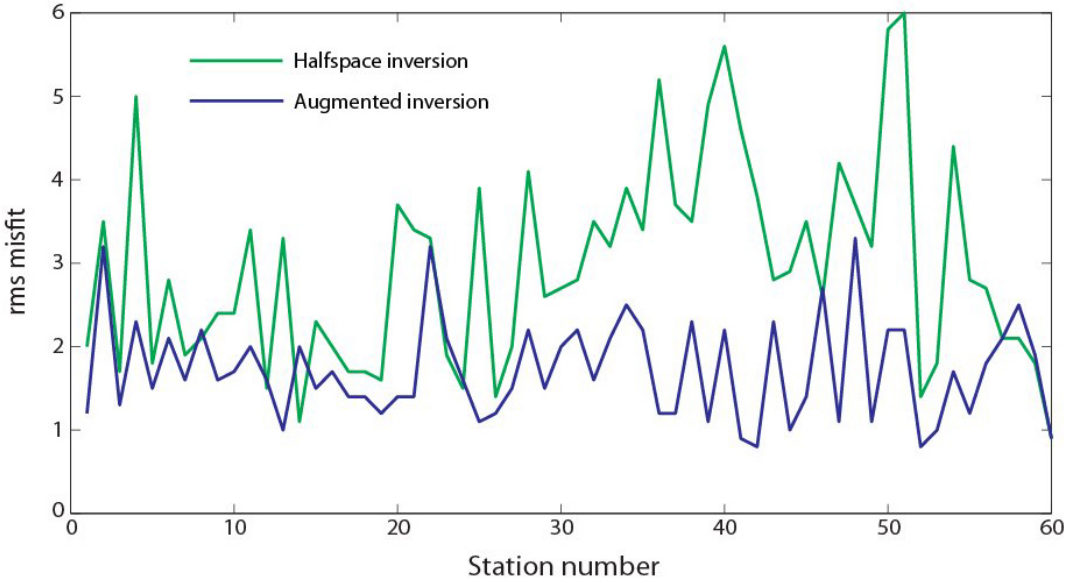

Extended Data Figure 4 | Plot of root-mean-square misfit against the 60 CAFE magnetotelluric stations for the TM/TE/tipper models. The blue line shows root-mean-square misfit by station for the halfspace model (without a tear or initial resistivity set for the upper slab), and the green line shows the same for the augmented model (using a tear at the top of the slab and imposing initial resistivity for the upper part of the slab). The overall root-mean-square misfit values were 3.08 for the halfspace model, and 1.89 for the augmented model.